

ShiD&namics of a Flexible Superhydrophobic Surface during a Drop Impact

Jeong-Hyun Kim^{1, 2*}, Jonathan P. Rothstein³, and Jessica K. Shang²

¹School of Engineering, Brown University, Providence, RI 02912, USA

²Department of Mechanical Engineering, University of Rochester, Rochester, NY 14627, USA

³Department of Mechanical and Industrial Engineering, University of Massachusetts, Amherst, MA 01003, USA

*Corresponding author: jeong-hyun_kim@brown.edu

Abstract

In this study, coupled dynamic responses of flexible superhydrophobic surfaces during a drop impact were investigated with position sensing and high-speed imaging. A smooth PDMS surface was spray coated with commercially available superhydrophobic paint particles. The influence of initial and subsequent impacts of a water droplet on the surface dynamics was studied at various natural frequencies of the surface ($50 < f_s < 230$ Hz) and Weber numbers (2 < We < 90). We discovered that the flexible superhydrophobic surface was deflected twice during contact of the droplet by an impact force of the droplet as well as its reaction force during recoil. The magnitude of the droplet reaction force was estimated to be comparable to the droplet impact force. As the Weber number increased, however, the influence of the droplet reaction force on the surface displacement was attenuated because of the instability of the droplet rim. The contact time of the droplet and surface dynamics were found to be dependent on the phase of the surface. The contact time was reduced as much as 7% when a completion of the droplet spreading matched to the upward motion of the surface. One of the two local minima of the surface position observed during the contact of droplet was diminished by matching the instance of the droplet reaction force to the



reaction force on dynamics of flexible superhydrophobic surfaces.

Keywords

Droplet reaction force, fluid-structure interaction, superhydrophobic surfaces

1. Introduction

When water contacts a superhydrophobic surface, the combination of chemical hydrophobicity of the surface and micron/nanometer-sized structures on it entraps air between the structures of the surface. The resulting heterogeneous solid-air-water interface on the superhydrophobic surface leads to a static advancing contact angle of $\theta_4 > 150^\circ$ and contact angle hysteresis of $\theta_H \approx 5^\circ$. This particular wetting condition makes water droplets bead up and roll easily across the surface. The reduced interaction between the water and the surface promises benefits such as self-cleaning, anti-icing, anti-fouling, and frictional drag reduction. However, elasticity of the superhydrophobic surfaces has not been characterized sufficiently even though superhydrophobic surfaces found in nature such as plant leaves, insect wings, gecko skin, and feathers are flexible.

The deformation of a water droplet impacting a rigid superhydrophobic surfaces is due to the interplay between inertia and capillary forces which can be described by the Weber number, $We = \rho U_0^2 D_0 / \gamma.^{18, 19} \text{ Here, } \rho \text{ is the density of water, } U_0 \text{ is the drop impact velocity, } D_0 \text{ is the initial droplet diameter, and } \gamma \text{ is the surface tension of water. At moderate Weber numbers,}$

AIP
Publishing

droplet spread into a pancake-like shape. The maximum spreading diameter scales as $D_{\text{max}} / D_0 \propto We^{1/4}$. During retraction, the droplet regains most of its initial kinetic energy with little viscous dissipation across the surface. This surface-to-kinetic energy conversion results in a complete rebound of the droplet which resembles a Worthington or Rayleigh jet. 20,22

On a flexible superhydrophobic surface, dynamics of the droplet will depend on surface properties. The impact force of the droplet, which scales as $F \square \rho U_0^2 \pi D_0^2$ 23, excites the flexible surface to vibrate at its first-mode natural frequency, $f_s = (1/2\pi)\sqrt{k_s/m_s}$. ²⁴⁻²⁶ Here, m_s is effective mass and k_s is flexural rigidity. During spreading, the initial kinetic energy of the droplet converts to elastic energy of the flexible surface and the surface energy of the droplet. ^{24, 25} The elastic energy stored in the flexible surface plays an important role on the dynamics of the droplet with the phase of the surface. When the natural frequency of the surface is lower than the droplet frequency, $f_s < f_d$, the spreading and recoil of the droplet occur while the surface is moving downward. 24 The droplet frequency, f_d , is defined by the reciprocal of an droplet oscillation period, $1/t_c$. Here, t_c is the theoretical contact time of the droplet, $t_c = 2.6 \left(\rho D_0^3 / 8\gamma\right)^{1/2}$, depending on the initial droplet size and its density and surface tension. 18, 20, 22 Under this circumstance, the elastic energy of the surface is internally dissipated through vibration and is not transferred to the droplet. This leads to a decrease in the maximum spreading diameter, D_{\max} , and suppression of droplet fragmentation. ²⁴ Furthermore, the maximum deformation of the droplet does not follow the classic scaling relationship for rigid superhydrophobic surfaces, $D_{\rm max}$ / $D_{\rm 0} \propto We^{1/4}$. ^{20, 21} When the upward motion of the flexible surface coincides with when the



blishids plet starts to recoil, $f_s \approx f_d$, the vertical momentum of the surface transfers kinetic energy to the droplet. In this scenario, the pancake-shaped droplet is lifted off from the surface, resulting in a contact time reduction and an enhanced restitution coefficient. ²⁴⁻²⁶ As the natural frequency of the surface increases further, $f_s > f_d$, the time of the maximum surface deflection is less than the maximum spreading time, $U_{spr} = D_0 / U_0$. The stored elastic energy of the surface returns to the droplet and participates in the droplet spreading dynamics. No difference in D_{max} / D_0 was observed compared to the rigid case. ^{27,28}

In recent studies, a high-speed camera and a light source were aligned with the flexible surface to image droplet dynamics and measure substrate deflection. However, to capture the region of interest, such imaging techniques are limited to measuring relatively large displacements, 0.1 to 1mm. In this study, we will investigate the coupled dynamic response of flexible superhydrophobic surfaces with high-speed imaging and a position sensing detector, which can resolve displacements of a few microns ($<2\mu m$). The presence of the reaction force of the droplet during retraction and its role on the surface dynamics will be revealed for the first time in this paper.

2. Experiments

2.1 Fabrication of flexible surfaces

The flexible hydrophobic surface was fabricated with Polydimethylsiloxane (PDMS, Sylgard 184 Dow Corning) using a standard soft lithography method.²⁹ The PDMS was created with a mixing ratio of 8 parts base to one part curing agent, by weight. The PDMS was cured on a six-inch silicon



surfaces was estimated to be $E = 2.5 \times 10^6$ Pa based on the mixing ratio of 8:1.³⁰ To produce the superhydrophobic surface, commercially available superhydrophobic paint particles suspended in a hydrophobic fluorothane resin (WX2100, Cytonix Co.) were deposited on the smooth PDMS surface. The paint particles formed aggregate hierarchical structures consisting of micron and nanometer-sized features on the surface. ^{5,31} The static advancing contact angle was measured to be $\theta_A = 150.2 \pm 0.7^\circ$ with the contact angle hysteresis of $\theta_B = 4.8 \pm 0.8^\circ$.

2.2 Deflection setup

The hydrophobic (uncoated) and superhydrophobic (coated) PDMS samples were cut into rectangular beams that were 40mm long, 32mm wide, and 1mm thick. The surfaces were supported on both ends and clamped in place with two binder clips, whose compressive force was distributed over two aluminum plates laid on the ends (Figure 1). Before each experiment, the horizontal image of the surface was taken by the high-speed camera and analyzed with ImageJ to verify that the surface was free of distortion and initial deflection.

To measure time-varying displacement of the surfaces, the optical deflection technique was utilized as shown in Figure 1. A laser spot which was created by a 5mW laser diode ($\lambda = 650nm$) was magnified by 0.5 and reflected upwards to the center point of the surface. The laser spot was reflected from a thin reflective layer deposited on the underside of the surface and imaged with a convex lens to hit the active area of a 1D silicon photodiode of a position sensing detector (PSD, On-Trak Photonics, Inc). The calibration of the PSD was verified by a micrometer which was placed in the same optical path as the surface. The PSD output was amplified by a position sensing



Publishing lifter (OT-301, On-Trak Photonics, Inc) and collected by a data acquisition board (National Instruments) with a sampling rate of 10kHz.

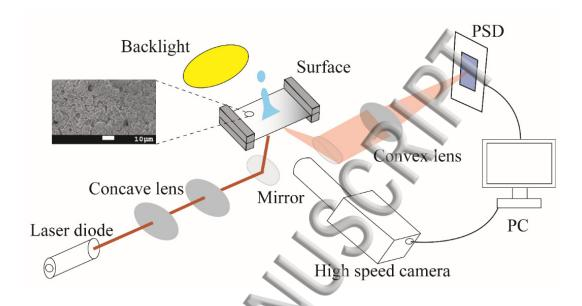


Figure 1: Schematic diagram of the experimental setup

Before each droplet experiment, the properties of the surfaces were quantified by an impulse exerted on the surface by a screwdriver with hexagonal ball end. An example for the dynamic response of the flexible superhydrophobic surface is shown in Figure 2. The displacement of the surface decreases exponentially as a function of time, following a second-order damped harmonic oscillator. The vibration frequency, f_s , of the measured surface deflection was calculated from a fast Fourier transform as shown in inset of Figure 2. The natural frequency of the flexible, untensioned hydrophobic and superhydrophobic surfaces was calculated to be 56Hz and 54Hz, respectively. The damping ratio of the surfaces was calculated as $\zeta = \ln \left| \delta_1 / \delta_2 \right| / 2\pi$, where $\ln \left| \delta_1 / \delta_2 \right|$ is the logarithmic decrement.



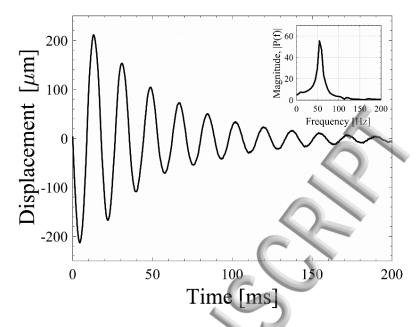


Figure 2: Displacement of the flexible superhydrophobic PDMS surface (untensioned) as a function of time when an impulse force is applied at t = 0. Inset indicates frequency distribution of the surface deflection.

To investigate the influence of the surface phase, ϕ_s , on the droplet and surface dynamics, the natural frequency of the superhydrophobic surface, f_s , was varied by applying a longitudinal tension and maintaining the length of the surface, L=40mm. The extension ratio of the surface, $\varepsilon=(l_1-l_0)/l_0$, was calculated by measuring longitudinal and transverse strains of a square drawn on the surface. Here, t_0 is the initial length of the square and t_1 is the length after stretching. As seen in Figure 3, the natural frequency of the surface increased linearly with the longitudinal extension ratio. In this study, we consider frequencies of $50 < f_s < 230$ Hz. At the highest frequency studied ($f_s = 230$ Hz), the extension ratio was measured to be 13% in the longitudinal direction and 6% in the transverse direction, consistent with a Poisson ratio of 0.5 expected of polymers. Beyond $f_s = 250$ Hz, the coating of superhydrophobic paint particles on the surface cracked so wettability of the surface was not uniform and could not be considered.



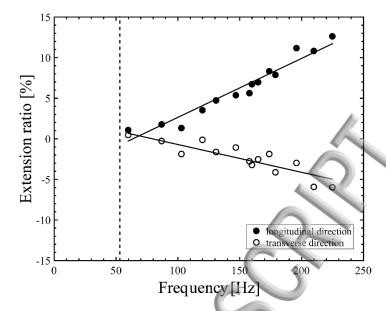


Figure 3: Variation of the extension ratios for the superhydrophobic PDMS surface as a function of natural frequency of the surface. The solid lines are linear square fits to the data. The dotted line indicates the frequency for the surface without tension.

2.3 Droplet force estimation

To better understand the surface dynamics as a function of time, we estimated the external force applied by the droplet to the surface, F(t), by using the second-order differential equation, $\ddot{\delta}(t) + 2\zeta \omega_s \dot{\delta}(t) + \omega_s^2 \delta(t) = F/m_s$, where $\delta(t)$ is the measured displacement of the center point of the surface, Here, $\omega_s = 2\pi f_s$ is the angular frequency of the surface, and $m_s \left(=k_s/\omega_s^2\right)$ is the effective surface mass. To find the flexural rigidity, k_s , of the surface and eventually estimate the effective mass, m_s , static deflection measurements were conducted at the center of the surface using ball bearings with masses of 0.07g, 0.26g, 0.44g, and 1.05g. For the untensioned surface, k_s was found to be 42.7N/m and m_s was found to be 0.38g. A zero-phase digital filtering technique was used to smooth high-frequency noise in the deflection data with a low-pass filter. A passband



shifts uency was set as 360Hz which was two times the higher frequency observed in the surface deflection as will be shown in Figure 4(a), and a stopband frequency was set as 720Hz.

2.4 Drop impact setup

A single water droplet with a diameter of $D_0 = 2.80 \pm 0.03$ mm was released from a syringe needle at a known height, H=40mm, and impacted the center of the surface. The impact velocity of the droplet was measured to be $U_0 = 0.72 m/s$, corresponding to We = 20. The droplet spreading and retraction dynamics on the surfaces were recorded with a high-speed camera (NAC HotShot CC) recording at a rate of 3000 frames/s. The impact location of the droplet was controlled by a two-dimensional droplet positioning system and monitored by the high-speed camera before each experiment to minimize variance of the drop impact location. The deflection of the surfaces was measured simultaneously with the high-speed imaging.

3. Results and discussion

3.1 Surface and droplet dynamics of untensioned flexible surfaces

3.1.1 Initial impact of the droplet

The time-varying displacements of the center of the flexible hydrophobic and superhydrophobic surfaces are shown in Figure 4(a). The displacement of both surfaces was initiated by the impingement of the droplet at t = 0ms. However, the dynamics of the surfaces depended on the surface wettability and corresponding droplet dynamics. The maximum deflection of the flexible hydrophobic surface was measured to be $\delta_{\text{max}} \approx 78 \, \mu m$ at t = 4ms, occurring after the droplet



Publishing hed the maximum spreading diameter, $D = D_{\text{max}}$, at t = 3.7ms as shown in Figure 4(b) and (c).

On the flexible superhydrophobic surface, the maximum deflection of the surface occurred earlier at t=3.4ms while the magnitude of the maximum surface deflection, $\delta_{\rm max}\approx 54 \mu m$, was about 30% smaller. The low contact angle hysteresis of the superhydrophobic surface, $\theta_{\rm H}\approx 10^{\circ}$, caused a shorter spreading time of the droplet, t=3.0ms, and a smaller maximum spreading diameter, $D/D_0=1.97$, compared to the hydrophobic surface (Figure 4(b) and (c)). As a result, a less initial kinetic energy of the droplet was transferred to elastic energy of the surface, in comparison with the hydrophobic case.

The calculated droplet forcing for the flexible surfaces are shown in Figure 5. The magnitude of the initial impact force of the droplet was calculated to be F =4.5mN at t = 0.1ms for the hydrophobic surface and F =4.2mN at t = 0.1ms for superhydrophobic surfaces, respectively. The impact force was estimated with a momentum transfer of the droplet upon impact, $F \sqcap \rho U_0^2 \pi D_0^2$; at We=20, the droplet impact force was calculated to be F =3.2mN 23 which is in good agreement with our results. It should be noted that the amplitude of the forcing function calculated in Figure 5 was contingent on the selection of parameters for the low-pass filter. The droplet impact force was estimated to be $F_{I,HS}$ = 4.4±0.3 and $F_{I,SHS}$ = 4.0±0.2 for the hydrophobic and superhydrophobic surfaces by changing the passband frequency of the lowpass filter between 260Hz and 460Hz.

As the droplet recoiled, the surface moved upward. During recoil, a three-phase contact line on the flexible hydrophobic surface was pinned and deflected until the local contact angle reached the dynamic receding contact angle, $\theta_{R,D} = 30^{\circ}$, while the droplet diameter was not significantly changed. As the droplet contracted to the impact point, a small liquid column on the

AIP Publishing

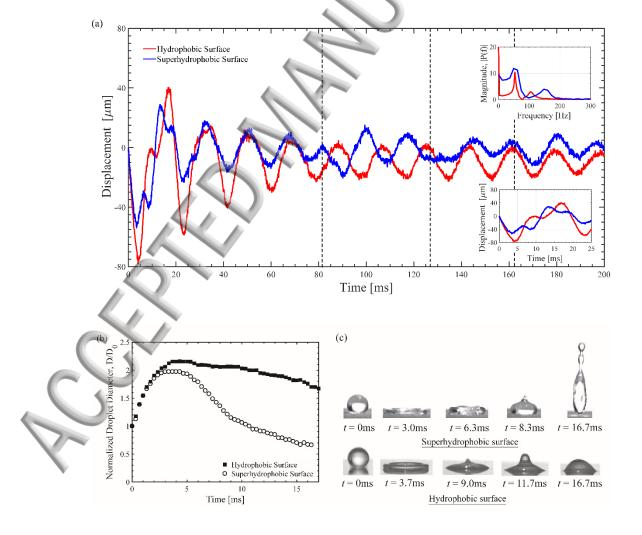
of the Worthington jet formed in droplet impact in liquids. The formation of the liquid column was accompanied by a small downward deflection of the surface (Figure 4(a), inset), countering the upward trajectory of the surface that was initiated at the beginning of recoil. This deflection implies that the droplet imparted a downward force as the liquid column was formed, and we will denote this as the droplet reaction force. The schematic diagram for the droplet reaction force will be shown in inset of Figure 5. When the liquid column collapsed at t = 11.7ms, the hydrophobic surface resumed its upward trajectory. After the initial interaction with the droplet, t > 20ms, the surface oscillated at its natural frequency ($f_s = 53$ Hz). The steady-state displacement was nonzero since the droplet remained pinned to the surface after impact. This result is in agreement with experimental observations for vibration of a hydrophobic cantilever beam after drop impact. ³² The higher frequency observed at $f_s = 107$ Hz in Figure 4 (a) was attributed to the deflection formed by the reaction force of the droplet.

A second downward deflection on the flexible superhydrophobic surface was observed at t=6.3ms during recoil (Figure 4(a), inset), while the droplet maintained a disk-like shape as shown in Figure 4(c). This implies that the larger dynamic receding contact angle, $\theta_{R,D}=140^{\circ}$, expedited the occurrence of the peak droplet reaction force. In contrast to the hydrophobic surface, the peak reaction force preceded the formation of the liquid column at t=8.3ms. Finally, the droplet detached from the surface at $t_c=16.6\pm0.1$ ms. The contact time was reduced by 6.7% relative to the rigid superhydrophobic surface, $t_c=17.8\pm0.2$ ms, when the flexible superhydrophobic surface was affixed to the aluminum plate. The dominant frequency of the surface deflection was measured to be in the range 49Hz < f < 62Hz, which was close to the measured natural frequency of the

AIP
Publishister

Publishing ace ($f_s = 54$ Hz). The droplet-surface interaction during the contact of the droplet led to a higher frequency peak at 148Hz < f < 161Hz.

As seen in Figure 5, the maximum reaction force of the droplet was calculated to be 4.8mN at t = 7.9ms and 4.9mN at t = 6.3ms for the hydrophobic and superhydrophobic surfaces, respectively. Hence the magnitude of the droplet reaction force was comparable to or even larger than the droplet impact force. Note that our analysis presumes the droplet reaction force can be integrated as a 1D point force at the center of the surface, where the droplet retraction is distributed over a finite area and is 3D. Therefore, the magnitude of the droplet force is an estimate, which requires non-intrusive force measurements (i.e., MEMS) in future work.





Publishifigure 4: (a) Time-varying displacement of hydrophobic and superhydrophobic surfaces. Inset indicates a frequency distribution of the surface deflection measured on both surfaces (top) and displacement detail for t < 25ms (bottom). The dotted lines represent subsequent impacts of the droplet on the superhydrophobic surface. For the superhydrophobic case, the frequency analysis was performed on data measured between 0ms < t < 81ms, before the second impact of the droplet. (b) Time evolution of non-dimensional diameter of the droplet impacting on hydrophobic (filled square) and superhydrophobic (circle) surfaces, (c) Droplet dynamics on hydrophobic (bottom line) and superhydrophobic surfaces (top line) as a function of time.

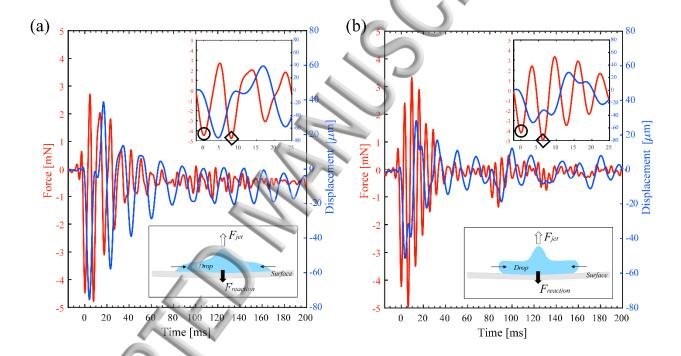


Figure 5: Estimated external force applied on the (a) hydrophobic and (b) superhydrophobic surfaces as a function of time. Insets show a schematic diagram to show the droplet reaction force on the flexible surface (bottom) and the force and deflection for t < 25 ms (top). The maximum impact and reaction forces are highlighted by solid circle and diamond symbols, respectively. The uncertainty in the force was estimated to be 0.1 mN by calculating the RMS value of the force for the times when there is no-forcing on the surfaces (400 ms < t < 1000 ms, not shown in the figure).



Subsequent impact of the droplet

After the droplet detached from the superhydrophobic surface, the rebounding droplet impacted the surface again at t=82ms, 127ms, and 162ms, indicated by dotted lines in Figure 4(a). The instance and location of the subsequent impacts varied, likely due to slight variations in the dynamics of the rebounding droplet in air and daughter droplet formation after recoil. Thus, surface dynamics after the additional impact of the rebounding droplet were determined by the droplet impact force, the stored elastic energy of the surface and the surface phase. Here, the surface phase is defined as the phase of the surface vibration when the droplet impacts on it (i.e., the surface phase is always zero, $\phi_s = 0^\circ$, at the initial droplet impact at t=0. The surface phase is $\phi_s = 90^\circ$ when the surface reaches the maximum deflection.) We will focus on three subsequent impacts of the droplet that corresponding surface displacement was noticeable.

At the time of the second impact of the droplet at t = 82ms, the surface was moving upwards $(\phi_s \Box 180^\circ)$, and the droplet was out of phase with the surface. The droplet kinetic energy was large enough to drive the surface downward even though the droplet was out of phase with the surface as shown in Figure 4 (a). The second impact modified the surface dynamics from the decaying oscillation initially excited by the first impact. This observation coincides with the recent result that the manipulation of the surface vibration occurs when the droplet is out of phase with the vibrating flexible surface. ²⁶ The droplet force at the second impact was estimated to be F = 1mN (Figure 5(b)), which is roughly 25% of the initial impact force. For the third impact at t = 127ms, the droplet was also out of phase with the surface, which had a concave shape $(\phi_s \Box 90^\circ)$. This surface phase was the worst-case scenario for enhancing displacement; the droplet kinetic energy cancelled out the stored elastic energy of the surface. Hence, the impact of the droplet was



corresponding droplet force magnitude was estimated to be 15% initial impact force, F = 0.7mN. Lastly, for the fourth impact at t = 162ms, the droplet was in phase with the surface $(\phi_s \square 270^\circ)$, temporarily enhancing displacement.

3.2 Influence of surface vibrating frequency

As discussed in the previous section, the relationship between the droplet impact and the surface phase plays an important role on the surface dynamics. In this section, the role of the surface phase on the droplet and surface dynamics will be further discussed in the context of changing the natural frequency of the superhydrophobic surface. The droplet spreading time was constant at t=3.3ms for every natural frequency studied, but this time corresponds to a different phase in the surface vibration depending on the surface's natural frequency. The droplet spreading time relative to surface phase for surfaces of varying frequency is illustrated in the inset of Figure 6. Since the surface transfers momentum to the droplet, the phase of the surface at the instant the droplet begins to recoil can change the contact time. We find that indeed the contact time can be manipulated by changing the surface vibrating frequency, as shown in Figure 6. When the completion of the droplet spreading was coupled to the upward motion of the surface in $50Hz < f_s < 100Hz$, the elastic energy of the surface was transferred to the kinetic energy of the droplet.^{25, 26} As a result, the contact time was reduced by as much as 7% compared to the rigid superhydrophobic surface. Beyond $f_s = 100$ Hz, the contact time gradually increased since less of the stored elastic energy of the surface was transferred to the droplet. Finally, at the critical surface phase of $\phi_s = 270^{\circ}$, the contact time reached a plateau at $t_c \sim 19 ms$, leading to a 7% contact time enhancement. This



Publishids endence of contact time on surface phase was recently reported on the drop impact on the vibrating superhydrophobic surface 26 . In their study, however, the contact time reduction was only observed at moderate Weber number of We = 50 to 60^{26} since their previous study showed that the contact time was only reduced above $We = 40^{25}$ Our measurements, however, show that the contact time can be reduced at low Weber numbers, We = 20, with a clear dependence of the contact time on the surface phase.

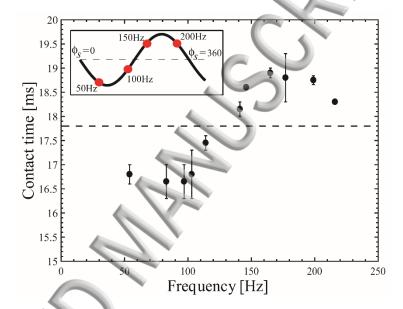


Figure 6: Contact time as a function of the natural frequency of the superhydrophobic surface. Inset shows a phase of the surface (solid line) and the time when the droplet reaches the maximum spreading diameter at the natural frequency of 50, 100, 150, and 200Hz (red circles).

In addition, the displacement of the flexible superhydrophobic surface was affected by the natural frequency of the surface. Time-varying displacements of surfaces of 6 different natural frequencies are shown in Figure 7. As the surface became stiffer with increasing surface frequency, the magnitude of surface deflection decreased, and subsequent droplet impact was not clearly detected in the surface deflection. However, the initial surface dynamics varied depending on the



lishing when the reaction force of the droplet occurred. As seen in Figure 7 (a) and (b), the additional deflection contributed by the droplet reaction force around t = 10ms was clearly observed until f_s =103Hz when the droplet reaction force was out of phase with the surface. Beyond the critical surface phase of 270°, the reaction force was applied when the surface was moving downward, and so the additional deflection was not apparent as shown in Figure 7 (d) and (e). As seen in Figure 7 (d), a possible beating-like surface displacement was observed when the droplet reaction force was coupled with the downward motion of the surface. This deflection seems to come from a slight difference between a higher mode resonance frequency of the droplet and the natural frequency of the surface. To make sure our postulate, the droplet mode frequencies were calculated based on the literature.³³ The n-th order resonance frequency of the oscillating droplet is expected to be $f_n = \sqrt{\frac{n(n-1)(n+2)\gamma}{4\pi^2 \rho R^3}}$. Here, *n* is the oscillating mode, γ , ρ , and *R* is the surface tension, density, and radius of the droplet, respectively. With the parameters of the droplet we used, the mode frequencies were calculated to be $f_2 = 72.9Hz$, $f_3 = 141.2Hz$, and $f_4 = 218.8Hz$. For the Figure 7(d), the surface vibrating frequency ($f_3 = 146Hz$,) was very close to the droplet's 3rd order frequency ($f_3 = 141.2Hz$,). However, the mechanism for this phenomenon is still unclear and will be investigated in a follow-up study.

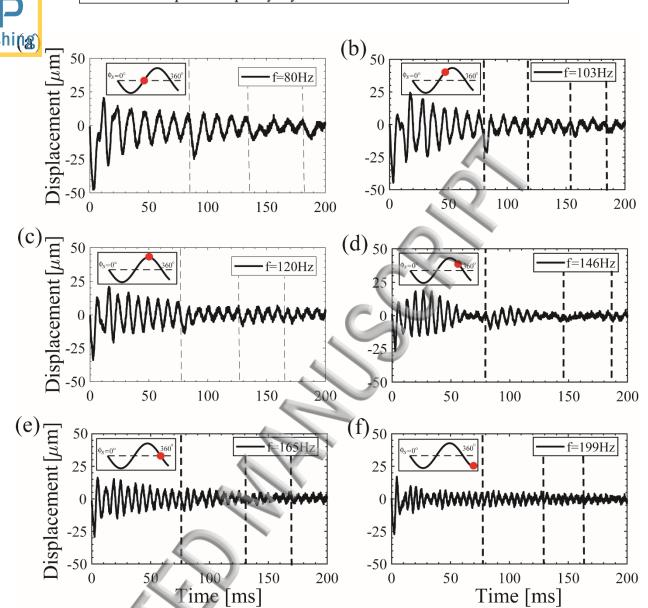


Figure 7: Time-varying displacement of the flexible superhydrophobic surfaces with natural frequency of (a) f = 80Hz, (b) f = 103Hz, (c) f = 120Hz, (d) f = 146Hz, (e) f = 165Hz, and (f) f = 199Hz. Inset shows a phase of the surface (solid line) and the time when the droplet reaction force occurs (red circles).



Influence of Weber number

Lastly, the dynamic response of the untensioned flexible superhydrophobic surface (f_s =54Hz) was investigated by changing the drop impact velocity (or equivalently, the Weber number). Surface displacements at three Weber numbers are shown in Figure 8 (a). The magnitude of the deflections generated by the droplet impact and reaction forces will be denoted as δ_{impact} and $\delta_{reaction}$, respectively. As the Weber number increased, the magnitude of δ_{impact} and $\delta_{reaction}$ during contact of the droplet (t < 10ms) increased, while the timing of those deflections remained almost constant. If the maximum surface deflection is assumed to be linearly proportional to the droplet impact force, δ_{impact} should scale with U_0^2 . As shown in Figure 8 (b), however, δ_{impact} scales as $We^{0.37}$, and hence $\delta_{impact} \sim U_0^{0.75}$, a much weaker dependence on the drop impact velocity. The reaction force-induced deflection, $\delta_{reaction}$, followed a similar scaling up to We=40. For We>40, however, the periphery of the droplet became unstable and airborne during droplet spreading. As the Weber number increased further, satellite droplets were formed around the rim of the main droplet (We~70). Thus, the main droplet regained less initial kinetic energy during recoil, resulting in a weaker dependence of $\delta_{reaction}$ on Weber number for We > 40. These results confirm the presence of the droplet reaction force on the droplet-surface interaction as well as its effect on the surface dynamics with changing the Weber number. Note that the relationship between the magnitude of the maximum deflection and Weber number depends on the surface properties including the flexural rigidity (EI) and natural frequency of the surface (f_s) . However, the variation of the scaling with changing the surface properties needs a variety of data set to generalize and is not a focus of the present study.

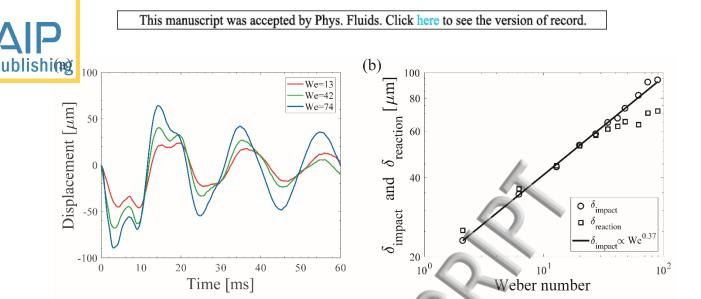


Figure 8: (a) Time-varying displacement of the flexible superhydrophobic surfaces for We=13 (red), 42 (green), and 74 (blue). (b) The maximum deflections induced by the impact force, δ_{impact} (circle), and the reaction force, $\delta_{reaction}$ (square). The solid line indicates a linear square fit to δ_{impact} .

Conclusion

In this study, we identified the presence of the droplet reaction force on the elastic superhydrophobic surface with clamped-clamped boundary condition using a position sensing detector (PSD) and high-speed imaging. This is the first direct measurement of the droplet reaction force in the literature. The flexible surfaces were displaced by the impact force of the droplet and reached a local minimum in its displacement as the droplet spreading was completed. A short time later, the surface experienced a second local minimum in its position due to a reaction force formed during droplet recoil. The droplet reaction force was estimated with a second-order harmonic oscillator, and its magnitude was found to be comparable to the estimated droplet impact force, $F \square \rho U_0^2 \pi D_0^2$.

To investigate the role of the droplet reaction force further, systematic measurements of surface displacements and droplet dynamics were conducted with changing the surface vibrating

ДIР Publishingu

blishing uency ($50 < f_s < 230$ Hz) and the drop impact velocity (2 < We < 90). The timing of the droplet reaction force changed the magnitude of the surface displacement and manipulated the time of the surface oscillation. When the droplet reaction force was coupled with the downward motion of the surface, one of the two local minima in the surface displacement diminished with the increased contact time. The contact time of the droplet increased as much as 7% at $160 < f_s < 200$ Hz. Also, the maximum deflection induced by the droplet reaction force depended on the outcome of the droplet spreading. As the rim of the droplet became unstable with increasing Weber number, the corresponding deflection for the droplet reaction force had a weaker dependence on Weber number. Our position sensing system was the most sensitive performed in the literature and allowed us to measure micron-resolution surface displacements at a high sampling frequency, consequently finding the presence of additional reaction force in the droplet-surface interactions. Our technique can expand the range of fluid-structure interaction problems that involve the regimes of high flexural stiffness and small displacements.

Supplementary Material

See supplementary material for the high-speed videos of the droplet impact dynamics on hydrophobic and superhydrophobic PDMS surfaces and detail of 2nd-order harmonic oscillator modeling.

Acknowledgement

The authors would like to offer special thanks to William Gorman for his valuable help in initial experimental setup and analysis of the data.



- 1. J. P. Rothstein, "Slip on superhydrophobic surfaces," Annual Review of Fluid Mechanics **42**, 89 (2010).
- 2. D. Quéré, "Wetting and roughness," Annual Review of Materials Research 38, 71 (2008).
- 3. F. Schellenberger, N. Encinas, D. Vollmer, and H.-J. Butt, "How Water Advances on Superhydrophobic Surfaces," Physical Review Letters **116**, 096101 (2016).
- 4. J.-H. Kim, and J. P. Rothstein, "Role of interface shape on the laminar flow through an array of superhydrophobic pillars," Microfluidics and Nanofluidics 21, 78 (2017).
- 5. J.-H. Kim, P. H. Kavehpour, and J. P. Rothstein, "Dynamic contact angle measurements on superhydrophobic surfaces," Physics of Fluids 27, 032107 (2015).
- 6. M. A. Nilsson, and J. P. Rothstein, "The effect of contact angle hysteresis on droplet coalescence and mixing," Journal of Colloid and Interface Science **363**, 646 (2011).
- 7. M. A. Nilsson, and J. P. Rothstein, "Using sharp transitions in contact angle hysteresis to move, deflect, and sort droplets on a superhydrophobic surface," Physics of Fluids **24**, 062001 (2012).
- 8. W. Barthlott, and C. Neinhuis, "Purity of the sacred lotus, or escape from contamination in biological surfaces," Planta **20**2, 1 (1997).
- 9. L. Cao, A. K. Jones, V. K. Sikka, J. Wu, and D. Gao, "Anti-icing superhydrophobic coatings," Langmuir 25, 12444 (2009).
- 10. J. Genzer, and K. Efimenko, "Recent developments in superhydrophobic surfaces and their relevance to marine fouling: a review," Biofouling **22**, 339 (2006).
- 11. C. Lee, C.-H. Choi, and C.-J. Kim, "Superhydrophobic drag reduction in laminar flows: a critical review," Experiments in Fluids **57**, 176 (2016).



- ultrahydrophobic surfaces," Physics of Fluids **16**, 4635 (2004).
 - 13. R. J. Daniello, N. E. Waterhouse, and J. P. Rothstein, "Drag reduction in turbulent flows over superhydrophobic surfaces," Physics of Fluids **21**, 085103 (2009).
 - 14. S. Srinivasan, W. Choi, K.-C. Park, S. S. Chhatre, R. E. Cohen, and G. H. McKinley, "Drag reduction for viscous laminar fow on spraycoated non-wetting surfaces," Soft matter **9**, 5691 (2013).
 - 15. D. Byun, J. Hong, J. H. Ko, Y. J. Lee, H. C. Park, B.-K. Byun, and J. R. Lukes, "Wetting characteristics of insect wing surfaces," Journal of Bionic Engineering **6**, 63 (2009).
 - 16. G. S. Watson, D. W. Green, L. Schwarzkopf, X. Li, B. W. Cribb, S. Myhra, and J. A. Watson, "A gecko skin micro/nano structure—A low adhesion, superhydrophobic, anti-wetting, self-cleaning, biocompatible, antibacterial surface," Acta biomaterialia **21**, 109 (2015).
 - 17. Y. Liu, X. Chen, and J. H. Xin, "Hydrophobic duck feathers and their simulation on textile substrates for water repellent treatment," Bioinspiration & Biomimetics **3**, 046007 (2008).
 - 18. A. L. Yarin, "Drop impact dynamics: splashing, spreading, receding, bouncing...," Annual Review of Fluid Mechanics **38**, 159 (2006).
 - 19. C. Josserand, and S. T. Thoroddsen, "Drop impact on a solid surface," Annual Review of Fluid Mechanics 48, 365 (2016).
 - 20. C. Clanet, C. Béguin, D. Richard, and D. Quéré, "Maximal deformation of an impacting drop," Journal of Fluid Mechanics **517**, 199 (2004).
 - 21. J.-H. Kim, and J. P. Rothstein, "Droplet Impact Dynamics on Lubricant-Infused Superhydrophobic Surfaces: The Role of Viscosity Ratio," Langmuir **32**, 10166 (2016).



- D. Richard, C. Clanet, and D. Quéré, "Surface phenomena: Contact time of a bouncing drop,"

 Nature **417**, 811 (2002).
 - 23. D. Soto, A. B. D. Lariviere, X. Boutillon, C. Clanet, and D. Quere, "The force of impacting rain," Soft matter **10**, 4929 (2014).
 - 24. T. Vasileiou, J. Gerber, J. Prautzsch, T. M. Schutzius, and D. Poulikakos, "Superhydrophobicity enhancement through substrate flexibility," Proceedings of the National Academy of Sciences **113**, 13307 (2016).
 - 25. P. B. Weisensee, J. Tian, N. Miljkovic, and W. P. King, "Water droplet impact on elastic superhydrophobic surfaces," Scientific Reports **6**, 30328 (2016).
 - 26. P. B. Weisensee, J. Ma, Y. H. Shin, J. Tian, Y. Chang, W. P. King, and N. Miljkovic, "Droplet impact on vibrating superhydrophobic surfaces," Physical Review Fluids **2**, 103601 (2017).
 - 27. R. E. Pepper, L. Courbin, and H. A. Stone, "Splashing on elastic membranes: The importance of early-time dynamics," Physics of Fluids 20, 082103 (2008).
 - 28. S. Mangili, C. Antonini, M. Marengo, and A. Amirfazli, "Understanding the drop impact phenomenon on soft PDMS substrates," Soft matter **8**, 10045 (2012).
 - 29. G. M. Whitesides, and A. D. Stroock, "Flexible methods for microfluidics," Physics Today **54**, 42 (2001).
 - 30. Z. Wang, A. A. Volinsky, and N. D. Gallant, "Crosslinking effect on polydimethylsiloxane elastic modulus measured by custom-built compression instrument," Journal of Applied Polymer Science 131, 41050 (2014).
 - 31. S. Moghtadernejad, M. Tembely, M. Jadidi, N. Esmail, and A. Dolatabadi, "Shear driven droplet shedding and coalescence on a superhydrophobic surface," Physics of Fluids **27**, 032106 (2015).



Publishing S. Gart, J. E. Mates, C. M. Megaridis, and S. Jung, "Droplet Impacting a Cantilever: A Leaf-Raindrop System," Physical Review Applied 3, 044019 (2015).

33. Y. Shin, and H. Lim, "Shape oscillation and detachment conditions for a droplet on a vibrating flat surface," The European Physical Journal E **37**, 74 (2014).



